Recurrent circuits encode visual center-surround computations in the mouse superior colliculus

Peng Cui[1†], Kuisong Song[2†], Dimitris Mariatos-Metaxas[1], Arturo G. Isla[3,4], Teresa Femenia[2], Iakovos Lazaridis[5], Konstantinos Meletis[1], Arvind Kumar[1,6] and Andreas A. Kardamakis[1,2,*]

Affiliations

[1]*Department of Neuroscience, Karolinska Institutet, Stockholm, Sweden*

[2]*Instituto de Neurociencias CSIC-UMH, San Juan de Alicante, Spain*

[3]*Tecnológico de Monterrey, Escuela de Medicina y Ciencias de la Salud, México*

[4]*Department of Neurobiology, Care Sciences and Society, Karolinska Institutet, Sweden*

[5]*McGovern Institute, Massachusetts Institute of Technology, Cambridge, USA*

[6]*Division of Computational Science and Technology. School of Electrical Engineering and Computer Science. KTH Royal Institute of Technology, Stockholm, Sweden*

[†]These authors contributed equally to this work
[*]Corresponding author, e-mail: akardamakis@umh.es

Abstract

Center-surround interactions underpin visual saliency computation, yet debate persists over whether subcortical visual circuits actively contribute or passively access this via descending cortical projections. To address this, we developed an optogenetic approach delineating visual center and surround zones of individual neurons in the superficial layer of the superior colliculus (SCs) solely using synaptic input arising from retinal ganglion cells (RGCs). Surround network activation of whole-cell recorded SCs neurons induced suppression of their RGC-driven center responses regardless of their cell-type. Notably, this modulation occurs through decreases in excitation rather than increases in inhibition. Cell-type-specific trans-synaptic and functional mapping in conjunction with large-scale modeling revealed a SCs-based circuit defined by two key motifs, highlighting the central role of local recurrent excitatory networks in generating surround inhibition. We propose that recurrent-based subcortical and cortical visual circuits have evolved to independently perform center-surround modulatory interactions, thus enabling parallel saliency computations across multiple levels.

Introduction

Enabling neurons to compare inputs to their receptive field with their immediate surround represents a fundamental and conserved computation (*1*, *2*). Termed 'surround modulation' and usually suppressive, it is widespread across sensory modalities such as vision (*3*), hearing (*4*), somatosensation (*5*), and olfaction (*6*). A typical example found across species is during size tuning of a visual neuron; the firing response initially increases when a stimulus is centered on its receptive field (*7*, *8*), but then decreases as the stimulus expands beyond this area (*9*–*12*). Such observations have been measured throughout the visual thalamocortical system in the lateral geniculate nucleus (*13*), primary visual cortex (*14*) and extrastriate cortex (*15*), as well as in retinotectal systems in the premammalian optic tectum (*9*, *16*, *17*) and superior colliculus (*8*, *10*). While center-surround interactions are known to originate in the retina, which has been extensively studied (*18*–*21*), little is known about the extent to which their modulatory effects are inherited by later stages of the visual hierarchy, such as in subcortical or cortical visual areas, or their relationship to each other (Fig. 1A).

Surround modulation relies on the rapid interplay between excitatory cells releasing glutamate and inhibitory cells releasing GABA (γ-aminobutyric acid). As intuition would suggest, surround suppression can be mediated by increases of levels of GABAergic inhibition, however, different neural systems may assume different mechanisms (*22*). For example, surround suppression in the primary visual cortex (V1) has been demonstrated to arise by decreases in levels of excitation rather than increases in synaptic inhibition (*23*). Determining this mode, along with its underlying neural implementation, is essential for uncovering the principles of saliency computations (*24*–*26*) required for visuospatial behaviors such as target selection in overt (*27*, *28*) and covert attention (*29*, *30*).

Here, we demonstrate how phylogenetically conserved circuits in the superficial layers of the superior colliculus (SCs) can trigger RGC-driven center-surround modulatory interactions essential for saliency even in the absence of cortical or any other extrinsic input, using similar recurrent mechanisms akin to those found in the neocortex. We devised a functional receptive field mapping method employing optogenetics and whole-cell electrophysiology to delineate center and surround zones of single SCs neurons in *ex vivo* using midbrain slices. By selectively activating these spatial zones in temporal sequences, we demonstrated how collicular surround suppression is mediated by decreases in excitation levels without increases in synaptic inhibition. This finding aligns with model predictions involving strong recurrent networks in the visual cortex (*31*, *32*), despite occurring in a structure that predates the evolution of the neocortex. To establish the circuit basis, we performed cell-type-specific trans-synaptic mapping to identify and quantify the underlying circuit motifs between local excitatory (*E*) and inhibitory (*I*) neurons in the SCs, revealing the presence of all connectivity patterns. This, in conjunction with large-scale computational modeling, unveiled the key role of local recurrent excitatory (*E*-*E*) connections, which engage in broader inhibitory interactions to generate surround suppression

across the SCs map of visual space. Finally, this could explain the observed functional decreases in the E/I balance in the surround when the center was active, confirmed through *in vivo cfos* induction, thereby validating a key model prediction.

Results

SCs space defined by recurrent excitatory and inhibitory circuit motifs

Local connectivity patterns between glutamatergic and GABAergic neurons define the nature of spatial antagonism in the SCs. Considering their comparable proportions (*33*) and their intermingling within the SCs, we opted for genetically restricted approaches, targeting excitatory neurons via the vesicular glutamate transporter 2 (vGluT2) and inhibitory neurons via the vesicular GABA transporter (vGAT), to accurately target and classify them based on their neurotransmitter. We performed retrograde trans-synaptic mapping from vGluT2 and vGAT neurons to identify their monosynaptic and presynaptic sources of excitatory and inhibitory input to ascertain whether the SCs uses direct connections of surround inhibitory neurons with center neurons, indirect connections using inhibitory center neurons targeted by excitatory surround neurons, or a combination of both.

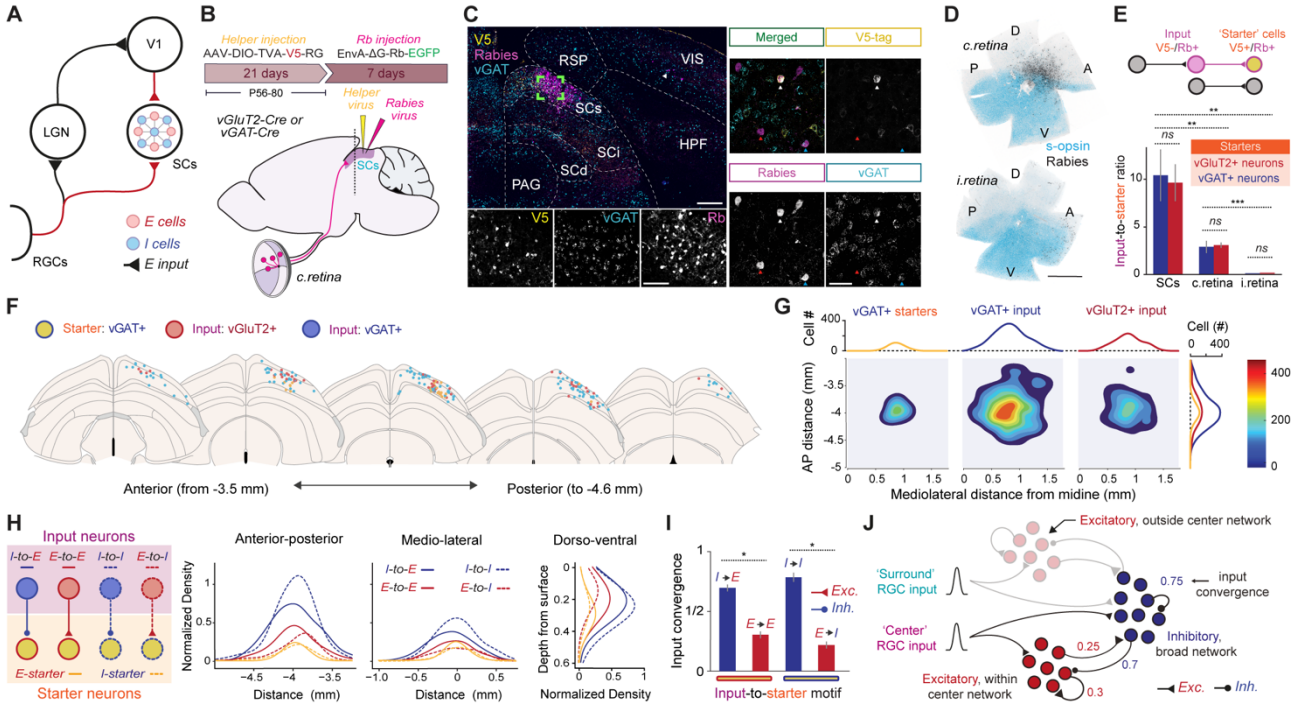

Fig. 1: Connectivity between local excitatory and inhibitory motifs in SCs space

(A) Interconnectivity of the early visual system originating with the retina. Red arrows highlight the main sources of excitation arising from direct retinal ganglion cells (RGCs) and indirect visual cortical (V1) input that target local excitatory (*E*) and inhibitory (*I*) neurons in the superficial layer of the superior colliculus (SCs).

(B) The helper virus AAV-DIO-TVA-V5-RG expresses the rabies glycoprotein (RG), and a fusion of the TVA receptor with the V5 tag. The RG-deleted rabies virus Rb, pseudotyped with EnvA, expresses EGFP. The AAV helper virus was first injected into vGluT2-Cre (N = 3) and vGAT-Cre (N = 3) mice and 3 weeks later the Rb-EGFP was delivered in the same location in the SCs.

(C) Left: coronal section of the midbrain of a vGAT-Cre animal with emphasis on initial injection site where expression of the V5 tag (in yellow) should be restricted to and not beyond the SCs layer. Subsequently,

EGFP-expressing neurons are a result of Rb-transfection (magenta). Scale bar: 300 µm. Insets below show colocalization of the enlarged area (green box). Scale bar: 100 µm. Right: RNAscope ISH for vGAT (for vGluT2, *see* Fig. S1) revealed the identity of Rb-EGFP input neurons while confirming starter neuron cell-types. White arrows indicate starter neurons, whereas red and blue show excitatory (*E*) and inhibitory (*I*) input neurons, respectively. Scale bars: 50 µm.

(D) Contralateral and ipsilateral retinas showing retinotopy of presynaptic Rb-EGFP RGCs (black). Counterstaining with s-opsin (light blue) reveals retinal orientation. Dorsal, D; anterior, A; ventral, V; posterior, P. Scale bars: 1000 µm.

(E) Top: starter neurons are identified based on the co-expression of the V5 tag and Rb-EGFP. Input neurons only express Rb-EGFP and provide monosynaptic and presynaptic input to the starter neurons. Bottom: Input convergence shows the ratio of input-to-starter neurons, i.e., *N*(input)/*N*(starter), arising from: i) within the SCs, ii) contralateral (*c.*), and iii) ipsilateral (*i.*) retina.

(F) Schematic depicting the dorsoventral and mediolateral location of starter and input neurons in five separate anterior-posterior (AP) coronal sections of the SCs layer in a vGAT-Cre animal.

(G) Contour plot showing the spatial distribution of *E* and *I* input neurons to *I* starter neurons in the AP and medio-lateral (ML) dimensions across the SCs (for case shown in **F**).

(H) (Left to right) Schematic of all possible motifs between input and starter neurons. The next three panels show the quantitative relationship between the density of input neurons and starter neurons for *E* and *I* cell types across the three anatomical dimensions (AP, ML and DV). Solid lines depict data obtained from excitatory starters averaged from vGluT2-Cre animals (*N* = 3), whereas dashed lines show data obtained from inhibitory starters averaged from vGAT-Cre animals (*N* = 3). *See* Fig. S5e for the distributions obtained from individual animals.

(I) Quantitative cell-type-specific input-to-starter ratios (referred to as *input convergence*) reveal feedforward (i.e., *E-I* and *I-E*) and recurrent connectivity patterns (i.e., *E-E* and *I-I*) calculated by *n*(vGAT+)/*n*(Total) and *n*(vGluT2+) / *n*(Total) presynaptic input neurons. Comparison of means performed using a *t*-test.

(J) Schematic of the E/I connectivity in SCs network highlighting the concept between center and surround in context of retinal input.

Abbreviations: c., contralateral; *i.*, ipsilateral; *RGCs*, retinal ganglion cells; *LGN,* lateral geniculate nucleus; *VIS* (and *V1*), primary visual cortex; *SCs*, superior colliculus superficial layer; *SCi*, superior colliculus intermediate layer; *SCd*, superior colliculus deep layer; *RSP*, retrosplenial cortex; *PAG*, periaqueductal gray matter; *HPF*, hippocampal formation.

To trace local afferent input to vGluT2 and vGAT neurons restricted within the boundaries of the SCs layer, an AAV-DIO-TVA-V5-RG was microinjected (50 nL) into the SCs of adult (> P58) vGluT2- and vGAT-Cre mice (Fig. 1B and Fig.S1). This Cre-dependent AAV helper vector was designed to express the TVA receptor together with the engineered rabies glycoprotein (RG; *see* (*34*, *35*)) exclusively in either excitatory or inhibitory neurons depending on the mouse line used. The injection of the helper virus was delivered into the SCs layer to ensure that neurons expressing the RG would be located within the SCs layer, thereby minimizing spillover into the intermediate layers (SCi) as indicated by the green box in the coronal midbrain section of Figure 1C. Any cases where helper expression extended beyond the boundaries of the SCs were excluded from the analysis. Three weeks later, the enhanced green fluorescent protein (EGFP)-expressing EnvA-coated and G-deleted rabies (Rb; *see* (*36*)) viral vector was injected, targeting the same location in the SCs as the helper virus injection (Fig. 1B-C).

Neurons that were transfected with the Cre-dependent helper virus, as detected by V5 immunohistochemistry, which would also express Rb-EGFP were referred to as 'starter' neurons (Top, Fig. 1E). Therefore, in experiments involving vGluT2-Cre animals (*N* = 3), vGluT2+ excitatory cells served as starter neurons, while in experiments with vGAT-Cre animals (*N* = 3), vGAT+ inhibitory cells

154 were the starter neurons. On the other hand, cells labeled solely with Rb-EGFP, without the presence
155 of the V5 tag, were classified as 'input' neurons, providing monosynaptic input to the starter neurons
156 (Fig. 1C-E). Rather than performing a whole-brain input analysis in the SCs (*see* (*37*)), we focused on
157 the local connectivity between vGluT2+ and vGAT+ neurons confined within the SCs. We quantified the
158 total number of presynaptic input neurons (Fig. 1E; *see* also Fig. 1H) and examined the spatial
159 distribution (Fig. 1F-G) onto each other within the SCs, as well as long-range inputs arising from both
160 retinas.
161
162 We measured a similar number of inputs per vGluT2+ and vGAT+ starter neuron from ipsilateral SCs
163 interneurons (mean ± s.e.m.: 9.5 ± 2 and 10.2 ± 2.8 cells, respectively) but also long-range inputs from
164 both contralateral (2.9 ± 0.3 and 2.8 ± 0.7 cells, respectively) and ipsilateral RGCs (0.07 ± 0.01 and 0.03
165 ± 0.02 cells, respectively). As expected, the retinotopic pattern is observed with contralateral RGC inputs
166 mainly originating in central regions and ipsilateral RGC input restricted to peripheral regions of the
167 retina (Fig. 1D), reflecting our systematic viral targeting of the middle region along the mediolateral (ML)
168 and anteroposterior (AP) axes of the SCs (Fig. 1B and 5A). To determine whether the Rb-EGFP+ input
169 cell types were excitatory or inhibitory, we performed RNAscope *in situ* hybridization (ISH) against
170 vGluT2 or vGAT, respectively (*see* Fig. 1C and Fig. S1). Neurons negative for vGAT, were positive for
171 vGluT2 and vice versa (Fig. S1). Figure S1 shows that co-staining Rb-EGFP+ cells with vGluT2 and
172 vGAT probes did not display colocalization, while nearly all detected input cells (269 out of 272 in $N = 2$
173 animals) were labeled by only one of these two probes.
174
175 The relative spatial distributions of vGluT2+ and vGAT+ starter and input neurons were determined by
176 counting the neurons expressing V5 and/or RV-EGFP and mapping their location onto the Allen
177 Reference Atlas coordinate system across the SC layer (Fig. 1F-G and Supplementary Fig. S1; *see*
178 Methods for details). In Figure 1F, a representative example of a vGAT-Cre animal is shown, illustrating
179 a small number of concentrated inhibitory starter neurons (V5+ and Rb-EGFP+; depicted as yellow dots)
180 together with a broader distribution of input neurons (Rb-EGFP+), which were further classified based
181 on their neurotransmitter type as excitatory (red dots) or inhibitory (blue dots). For all animals, we
182 determined the mediolateral (ML), anteroposterior (AP), and dorsoventral (DV) distribution using this
183 approach for each starter and input neuron, as well as their respective cell type classification (Fig. S1E).
184
185 The Gaussian kernel-based density plots in Figure 1G reveal the horizontal distribution patterns along
186 the ML and AP dimensions (*see* Methods) of the example shown in Figure 1F. Inhibitory starter neurons
187 (left panel in Fig. 1G) were observed to occupy a confined retinotopic area within the SCs, influenced
188 monosynaptically by a broader excitatory area (right panel in Fig. 1G), as well as an even broader
189 inhibitory area (middle panel), thereby, receiving visual input from RGCs located across larger retinal

190 regions. At peak density, the inhibitory starters were found to receive synaptic input from more than
191 double as many inhibitory input neurons establishing a motif of recurrent inhibition (Fig. 1H-I).
192
193 Using this approach applied in all animals (N = 6), we found that every possible motif between input and
194 starter neurons existed (Fig. 1H-I; *see* also Fig. S1E). In Figure 1H, color-coded solid lines represent
195 average spatial distributions using excitatory neurons as starters, while color-coded dashed lines
196 correspond to those from inhibitory starters (for each animal, *see* Fig. S1E). As expected, input neurons
197 always displayed higher normalized density distributions compared to their starter counterparts. Notably,
198 while *I-E* and *I-I* input-to-starter connections span a broader range on the ML, AP and DV axes, a stable
199 E/I ratio is maintained throughout the SCs, with no identifiable asymmetries arising from a specific
200 connection. By contrast to excitatory neurons, inhibitory inputs exhibited more connections with both
201 inhibitory starter neurons (78.8 ± 4.6%, n = 3, compared to 21.2 ± 4.6%, n = 3) and excitatory starter
202 neurons (69.2 ± 2.3%, n = 3, compared to 30.8 ± 2.3%, n = 3). Notably, about one third of excitatory
203 input neurons establish monosynaptic contact with excitatory starter neurons (second column in Fig. 1I),
204 thereby, establishing a local recurrent excitatory network that can be also triggered by monosynaptic
205 long-range RGC input (Fig. 1D; *see* also Fig. 3F). The summarizing cartoon in Figure 1J illustrates how
206 spatial distributions of cell-type-specific connectivity patterns (Fig. 1H) with input convergence ratios
207 (Fig. 1I) can outline the SCs circuit into RGC-based center and surround zones.
208
209 **Functional receptive field mapping of SCs neurons**
210 To provide the functional basis of this circuit configuration, we sought to trigger visual center and
211 surround interactions in an *ex vivo* experimental setting by using optogenetically-induced retinotopic
212 impulse patterns in midbrain sections of the SCs during whole-cell recordings (Fig. 2). By leveraging the
213 aligned topographic correspondence of the retinotectal pathway (*38*), we generated an input-dependent
214 visual field. We made it light-excitable by injecting an adeno-associated virus (AAV) intravitreally that
215 expressed ChR2 in RGCs of both wild-type C57BL/6NCrl (n = 22, N = 14) and vGAT-Cre (n = 7, N = 5)
216 mice (*see* top panel, Fig. 2A). To ensure sufficient expression of ChR2 across the SCs, homogeneous
217 pan-retinal expression of ChR2 was an essential prerequisite for trial inclusion (Bottom left, Fig. 2A);
218 partial expressions were not taken into consideration to minimize the risk of false positive surround
219 classification that could arise from lack of ChR2 expression. We mapped the receptive fields of single
220 SCs neurons (n = 29, N = 19), referred herein to as center zones (C), by detecting subregions that
221 triggered excitatory postsynaptic currents (EPSCs) in response to site-specific light patterns (Fig. 2B-
222 C), which would activate the retinotopically arranged ChR2-expressing RGC axonal terminals in coronal
223 SC sections along the medial-lateral and dorsal-ventral axes of the SCs (Bottom right, Fig. 2A).
224

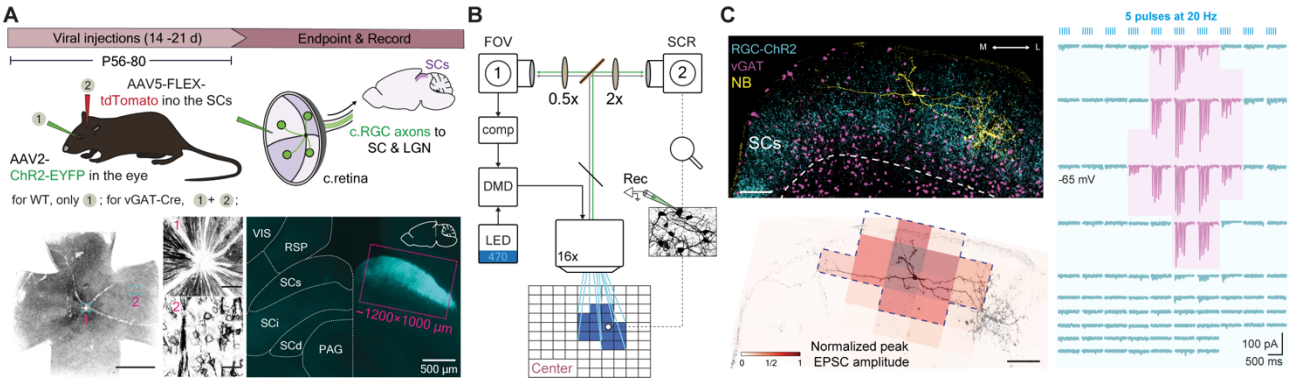

Fig. 2: Functional receptive field mapping of SCs neurons

(A) Top: Procedure showing expression of ChR2 in RGCs using an intravitreal viral injection of the vector rAAV2-hsyn-hChR2(H134R)-EYFP (in WT mice, $N = 14$) and unilateral labeling of contralateral SCs inhibitory neurons with the vector rAAV5-FLEX-tdTomato (in this case vGAT-Cre mice were used, $N = 5$). Bottom left: Inverted fluorescent image of whole retinal mount confirming homogeneous transfection of RGCs with ChR2-EYFP. Scale bar: 1200 µm. Insets show enlarged aspects of the optic disc (1) and individual RGCs (2). Scale bar: 25 µm. Bottom right: Coronal midbrain section with ChR2-expressing RGC axonal terminals seen occupying the SCs layers.

(B) A dual magnification setup for functional receptive field mapping of single cells. This enabled the simultaneous visualization of a large field of view (FOV) encompassing the SCs layer, and single cell resolution (SCR) for identifying center excitation zones using whole-cell recordings and patterned optostimulation via a digital mirror device (DMD). *See* also experimental procedures and Fig. S1-S4.

(C) Top left: a representative example of this approach applied to an inhibitory horizontal SCs neuron stained intracellularly with Neurobiotin (NB). Scale bar: 100 µm. The neuron responds with excitatory postsynaptic currents (EPSCs, shown in magenta) to a 20 Hz 5-light-pulse train delivered pseudo-randomly. Each trace comes from a single optostimulated rectangular area of 120×100 µm (shown on the right). Bottom left: reconstructed neuron is shown with the denoted excitation zone (dotted line), which is referred to as center, whereas the non-responsive areas as surround (S) zone.

Abbrev: c., contralateral; *comp*, computer; *Rec,* recording; *WT*, wild-type; *ChR2*, channelrhodopsin-2; *RGC*, retinal ganglion cell; *VIS,* primary visual cortex; *RSP*, retrosplenial cortex; *SCs*, superior colliculus superficial layer; *SCi*, superior colliculus intermediate layer; *SCd*, superior colliculus deep layer; *PAG*, periaqueductal gray matter; *LGN,* lateral geniculate nucleus.

Given the *a priori* unknown perimeter of each neuron's center zone, the surround zone (S) can exhibit significant spatial variability and extend over a wide area (Fig. 2B-C). To accurately cover each neuron's center zone and ensure a significant surround area, it was essential to create a sufficiently large field of view (FOV) that could accommodate their distinct morphologies. To do this, we used one-photon widefield optics via a low magnification objective (16×) while using an in-house built dual-focus visual inspection system to selectively magnify or demagnify the optical path (Fig. 2B). Demagnification (by 0.5×) captured a large field of view of > 1mm^2 that incorporated most of the SCs (magenta box in lower right of Fig. 2A), thus allowing for patterned micro-optostimulation of the entire visual layer. The other path diverted the light for magnification (by 2×), thereby achieving sufficient single cell resolution to visually target our neurons of interest for whole-cell recordings (Fig. 2B). This receptive field mapping approach allowed us to delineate spatial patterns defining center and surround regions of single neurons, which were subsequently used to selectively activate separately or in sequences during recordings. Figure 2C illustrates the center zone of a vGAT+ horizontal cell, which was determined by

263 measuring evoked EPSCs after optostimulation (5 impulses at 10 Hz) of a 10 × 10 grid covering the
264 FOV. The areas that evoked EPSC amplitudes exceeding 10-20% of the peak value (*see*
265 Supplementary Fig. S2) collectively formed an image pattern that were classified as the center, which
266 usually encompassed the soma and most of the dendritic processes (Bottom left, Fig. 2C; *see* also
267 Supplementary Fig. S2 and S5).
268
269 **Visual surround network activation modulates center excitability in the SCs**
270 Selective activation of this center zone always triggered short-latency compound EPSCs (mean
271 amplitude: 120.8 ± 15.5 pA) characterized by prominent multimodal peaks (*see* arrowheads in the
272 magenta trace in Fig. 3A), suggesting the presence of recurrent activity in addition to monosynaptic
273 excitatory RGC input (Fig. 3; *see* also Fig. 4C). Optostimulation of the center zone (control traces in
274 magenta) always resulted in an excitatory phase quickly followed by an inhibitory one (Fig. 3A-B). To
275 induce center-surround interactions, we first activated the surround using three different durations and
276 onsets (*see* dotted box in Fig. 3A). Light stimulation intensity was held constant for both the center and
277 surround zones. The surround-stimulation phases were terminated 20 ms before center-stimulation
278 onset to ensure adequate time for the build-up of surround-induced activity while allowing for signal
279 synchronization with the center-induced activity (cyan traces in Fig. 3A; *see* also Fig. S4D). Obviously,
280 within these experimental settings, simultaneous center and surround activation (akin to whole-field
281 stimulation) would mask any discernible effect the surround would have on the center. Comparing the
282 magenta and cyan traces in Fig. 3A reveals a distinct and consistent decline in center responsiveness
283 after surround activity, seen by a significant reduction in center-evoked EPSC amplitudes (~50%
284 decrease in this recorded cell) along with a concurrent decrease in the number of multimodal peaks. In
285 line with previous studies (*9*, *39*), these evoked EPSCs were rapidly followed (mean peak latency ±
286 s.e.m.: 5.9 ± 0.8 ms) by a feedforward inhibitory component (mean amplitude ± s.e.m.: 24.3 ± 5.0 pA)
287 observed near the equilibrium potential for glutamate-mediated excitation (0 mV, bottom of Fig. 3A), and
288 here we observe that it occurred regardless of the presence of a preceding surround. Holding potentials
289 shown in Fig. 2-3 (and Fig. S2-S3) are not corrected (NC) for the liquid junction potential, which was
290 determined to be ~10 mV.
291
292 The degree of surround modulation varied across different SCs neurons. Based on the intensity of the
293 reduction in center EPSC amplitude, the suppression was classified as mild, moderate or strong (Fig.
294 3A-B; strong: > 60%, n = 9/24; moderate: 20-60%, n = 10/24; mild: < 20%, n = 5/24). Figure 3B shows
295 the voltage and current traces of a stellate SCs interneuron that was subject to a strong surround
296 influence (*see* Fig. S3 and S5). When its surround was activated first, retinal input arriving to the
297 neuron's center zone (top and middle traces in Fig. 3B) was completely suppressed by an outward
298 current pulling its membrane potential toward the reversal for chloride-mediated $GABA_A$ (γ-aminobutyric
299 acid type A) inhibition (~69 mV; *see* bottom traces in Fig. 3B). Notably, the precise relative timing

between surround (t_s) and center stimulation onsets (i.e., -70, -40, or -25 ms) or surround stimulation duration (5, 20, or 50 ms) had little impact on the amplitude variance of surround-triggered inhibitory postsynaptic currents or on the relative impact of center modulation. This mainly stems from latency differences in signaling between center and surround, with surround *E* and *I* conductances peaking at average latencies of 20 and 28 ms, whereas center conductances peaked at 9 and 15 ms, respectively (Fig. S4d).

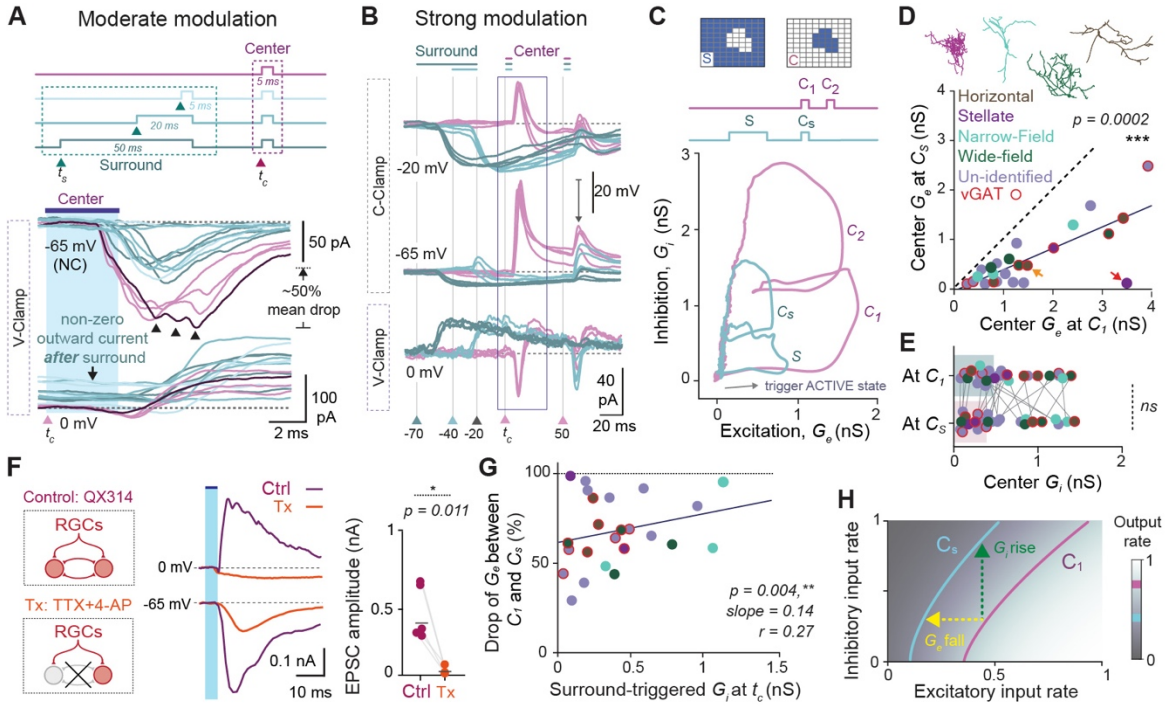

Fig. 3: Visual surround network activation modulates center excitability in the SCs

(A) Synaptic modulation between the center and surround zone of the neuron shown in (c). Top: Temporal patterns underlying surround and center interaction. Bottom: Individual traces of synaptic inward and outward currents evoked in response to center stimulation when recording at reversal equilibriums for $GABA_A$-chloride mediated inhibition and glutamatergic excitation (-65 and 0 mV, respectively). Arrowheads show EPSC recurrence in an individual trace (darker shade). Scale bar: 100 µm. Full traces in Fig. S2. Traces were not corrected (NC) for the offset created by the liquid junction potential, which was experimentally confirmed to be ~10 mV.
(B) Voltage traces revealing the strong modulation that the surround exerts on center activity in a stellate SCs interneuron. Voltage responses during surround followed by center (green traces) at two membrane holding potentials (-20 mV and -65 mV, top and middle, respectively) or during center alone (magenta). Bottom: Current traces when holding at 0 mV using the same condition.
(C) Plot of the inhibitory conductance as a function of the excitatory conductance in the neuron shown in (c) and (d). Arrow shows direction of process when neuron is activated.
(D-E) Comparison of synaptic excitatory **(D)** and inhibitory **(E)** conductances between conditions: center only (C_1) and center after surround (C_S). Color coding corresponds to morphologically or genetically identified SCs neuron cell-types. Orange and red arrows depict data points from neurons shown in (d) and (e), respectively. Top: Morphological reconstruction of the classic SCs subtypes (*see* Fig. S5 for details).
(F) Excitatory and inhibitory current recordings (at -65 and 0 mV) from SCs neurons (n = 5) were performed in response to center optostimulation of ChR2-expressing RGC axonal terminals. Bath application of 1 µM TTX and 100 µM 4-AP isolate monosynaptic RGC-triggered excitation while simultaneously abolishing

recurrent excitation and recruited inhibition. Mean evoked EPSC amplitudes ± s.e.m.: from left to right, for Ctrl: 0.40 ± 0.08 nA; for Tx: 0.02 ± 0.01 nA; p = 0.0072; Washout not shown for clarity.
(G) Modulation of center excitation plotted as a function of inhibitory conductance that is present at the time of center optostimulation (t_c).
(H) Schematic showing how the same level of response suppression can be achieved by either decrease in excitatory conductance or by increase in the inhibitory conductance. The gray colormap indicates a 2D input-output transfer function of a neuron as a function of normalized input excitation and inhibition. The two curved lines indicate iso-firing rate contours.
Statistical comparisons were performed as paired *t*-tests followed by Wilcoxon rank-signed tests. *Abbreviations: NC*, not corrected.

Surround network activation typically generated a variable combination of excitation and inhibition in terms of amplitude and timing. However, during the onset of center stimulation (t_c), only the inhibitory components persisted while surround-triggered excitation would elapse due to the relatively faster transmission of synaptic excitation. This can be seen by the non-null values of surround-triggered outward currents when holding at 0 mV at t_c (*see* arrows, Fig. 3A-B; *see* also Fig. S3). As expected, removal of surround input via pharmacological blockade of $GABA_A$ receptors using bath-applied gabazine (GBZ) transformed any input into seizure-like activity while saturating subsequent center response profiles (bottom traces in Fig. S3a).

To test how surround signaling can account for the observed modulation of center excitability, we calculated the theoretical contributions of excitatory (G_e) and inhibitory (G_i) synaptic conductances (*40*, *41*) during center only (magenta) and center-surround interaction (cyan) in Figure 3C. Here, the relationship between inhibition and excitation of the recorded neuron plotted in Figure 3A is shown during these two conditions (*see* also Fig. S4). Notably, consecutive center stimuli (C_1-C_2) reveal that inhibition can increase to nearly double the levels while simultaneously maintaining twice the levels of excitation compared to the significantly decreased levels evoked by surround-center stimulation (S-C_s). This result suggests that center-surround interactions reduce the persistence of both types of inputs. This was true for the majority of SCs interneuron cell types, with over half of them being classifiable based on either morphology (i.e., horizontal, wide-field, narrow-field, or stellate; for details, *see* (*42*)) or genotype (e.g., vGAT+). Figure 3D (*Top*) depicts representative reconstructions for each SCs cell-type (*see* Fig. S5 for quantification). We found that peak excitation (G_e: mean amplitudes of C_1: 1.7 ± 0.3 nS and C_s: 0.6 ± 0.1 nS with a mean percentage decrease of 62.3 ± 4.7%) and peak total conductance (G_t: mean amplitudes of C_1: 2.1 ± 0.3 nS and C_s: 1.2 ± 0.2 nS with an average percentage decrease of 40.6 ± 5.3%) of the center response was significantly reduced following surround network activation in all these recordings (Fig. 3D and Fig. S4), while no significant accompanying increase was observed on average to the center inhibition at peak G_t (Fig. 3E; mean amplitudes of C_1: 0.53 ± 0.08 nS and C_s: 0.55 ± 0.09 nS).

369 Figure 3F demonstrates the efficacy of the recurrent excitatory connection (*E-E)* by recording SC
370 neurons (*n* = *5*) in response to optostimulation of RGC terminals within their identified center zones in
371 the presence of 1 μM TTX and 100 μM 4-AP (washout *not shown* for clarity). Evoked EPSC amplitudes
372 were drastically reduced by about ~90%, with a small component persisting resulting from monosynaptic
373 RGC input (Fig. 3F, mean amplitudes ± s.e.m.: for Ctrl: 405.5 ± 81.1 pA; for Tx: 22.3 ± 11.0 pA). This
374 observation shows how a functional *E-E* connection can provide additional center-dependent excitatory
375 input (Fig. 1H-I; *see* also S1E), which may serve to amplify incoming retinal signals within the neuron's
376 center zone. Furthermore, the lack of observed outward currents (traces held at 0 mV) during this treated
377 condition (Tx) indicates the removal of recruited di- or oligo-synaptic inhibition, thereby exposing the
378 indirect functional impact of local *I-E* and *I-I* inputs onto single SCs neurons.
379
380 There are two explanations for this weakening of the center excitatory conductance: (i) inhibitory
381 conductances persisting at t_c, which might act linearly or non-linearly, and/or (ii) a lesser number of
382 active excitatory inputs contributing to the center response. Although a weak, yet statistically significant,
383 correlation was observed between the inhibitory conductance at t_c (mean amplitude ± s.e.m.: 0.46 ±
384 0.08 nS, p = 0.004, n = 24) and the reduction in the center peak excitation (Fig. 3G), the low slope value
385 indicates that synaptic inhibition can only account for a partial explanation of the observed decrease in
386 center excitation. The circuit configuration in Figure 1J supports the alternative suggesting robust
387 excitation reductions during center-surround interactions occur through removal of recurrent excitatory
388 amplification. The diagram in Figure 3H shows how surround suppression, represented by the decrease
389 in iso-firing rate contours (from magenta to cyan), can theoretically occur through drops in excitatory
390 firing rates without corresponding increases in inhibitory firing rates.
391
392 **Recurrent excitation is necessary for surround suppression**
393 To evaluate the contribution of each of the identified connections in Fig. 1 (i.e., *E-E, E-I, I-I,* and *I-E*) to
394 surround suppression in the SCs, we constructed a large-scale model consisting of 12,800 spiking
395 neurons to simulate the SCs layer. The model was constrained by the measured input convergence
396 ratios and spatial distributions (Fig. 1H-I and Fig. S1E) summarized in the cartoon in Figure 1J. To
397 quantify these network interactions, we used a spiking neuron model with conductance-based synapses,
398 which were connected to each other based on physical distance according to a Gaussian connectivity
399 kernel (see Table S3). Because we were interested in the contribution of different connections, we kept
400 the connection probability and distance-dependent connectivity kernel fixed and systematically varied
401 the connection strengths (*see* Table S4 for neuronal parameters; Table S5 for synaptic parameters;
402 Table S6 for network connectivity; and Table S7 for external input parameters). Consistent with
403 experimental findings (*43*), the network remained in an inhibition-dominated activity regime in which
404 inhibitory neurons displayed a higher background activity than excitatory neurons for all synaptic
405 strengths.

To mimic center activation, we triggered activity in 314 excitatory and 314 inhibitory model neurons in four conditions (Fig. 4A) and measured the evoked excitatory synaptic conductance in a randomly chosen neuron from the center region (Fig. 4C). First, the center neurons alone were stimulated (*see* #1 in Fig. 4A-B). As with our experimental recordings (*see* Fig. 3A), model center response patterns typically demonstrated multiple peaks, often characterized by a dual peak profile (green traces in Fig. 4C). The first peak is provided monosynaptically by glutamatergic RGC input and followed by a second peak reflecting center-induced activity in neighboring unstimulated excitatory neurons. As expected, the second peak depended mainly on the strength of recurrent excitatory connection (*E-E*) and was also found to covary with the strength of the *I-E* connection (Fig. 4D).

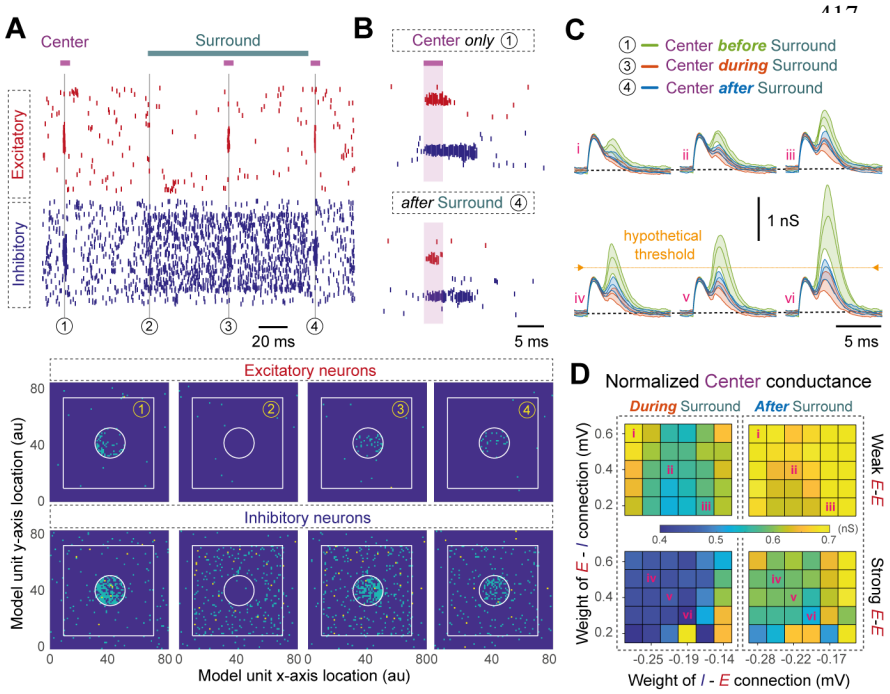

Fig. 4: Model predicts recurrent networks a key feature in visual surround suppression

(A) Network model simulation using E/I connectivity patterns summarized in Fig. 1J. Top: Raster of spiking activity from 6400 excitatory and 6400 inhibitory neurons with four stimulus conditions that are marked with vertical numbered lines that simulate experimental conditions shown in Fig. 1. Conditions *1:* center only before surround, *2*: surround only, *3*: center during surround, and *4*: center after surround. Bottom: Spatial arrangement of center and surround network response profiles during the 4 different stimulus impulse conditions. The square schematically shows the region in which neurons were placed on a square grid. Excitatory (top) and inhibitory neurons (bottom) within the white circle received inputs corresponding to the center stimulation. All the neurons in white square but outside the inner circle received inputs corresponding to the surround network. Each subplot shows activity measured within a bin of 5 ms. The entire simulation is shown in Fig. S6.
(B) Expanded network response of conditions 1 (top) and 4 (bottom) shown in **(A)**.
(C) Time courses of excitatory conductance of a center neuron. Each trace is an average of 20 trials and shading indicated 25%-75% quartiles. The first peak is generated with low-variance monosynaptic activation of direct retinal input whereas the second peak is a network effect generated by balanced recurrent excitation and recurrent inhibition. The connectivity parameters for these six examples are marked in inset (**D**) with Latin numerals.
(D) Normalized center conductance during and after surround stimulation. Each colormap shows normalized change in excitatory conductance (*see* Methods) in a center neuron (shown in inset **C**) as a function of recurrent excitation (top: weak connection; bottom: strong connection) and mutual connectivity weights between excitation and inhibition (x-axis: inhibition of excitatory neurons; y-axis: excitation of inhibitory neurons).

When center stimulation was immediately followed by a surround input (*see* #4 in Fig. 4A), the peak of the secondary response was determined by the mutual coupling between excitatory and inhibitory

456 neurons (blue traces in Fig. 4C). In line with our results presented in Fig. 3, the initial surround-induced
457 inhibitory conductance persisted after the removal of surround inputs, effectively attenuating the
458 secondary response to below threshold (yellow dotted line in Fig. 4C). This occurred because fewer *E*
459 and *I* neurons could respond beyond threshold to the center input (bottom panel in Fig. 4B). This was
460 further supported by the observation that secondary response attenuation was more pronounced when
461 center input coincided with the presence of surround input (red traces in Fig. 4C). Validation of this
462 prediction was not possible experimentally as center responses would prevail during the whole-field
463 stimulation, i.e. simultaneous optogenetic activation of center and surround zones (*see* #3 in Fig. 4A).
464
465 To quantify the contribution of individual circuit motifs, we normalized the center response during and
466 after surround network activation (columns in Fig. 4D) by the peak when only center input was delivered.
467 As expected, any increase in the *I-E* connection increased its attenuation, whereas *E-I* connectivity did
468 not have a strong effect on the attenuation of the secondary peak. Notably, increase in the strength of
469 recurrent excitation also increased the attenuation of the secondary excitatory conductance peak
470 (compare top and bottom panel in Fig. 4D). The effect of surround-triggered inhibition on center
471 excitation was larger when center input arrived in the presence of an active surround (left column in Fig.
472 4D). Overall these results demonstrate that reduction in center excitation during surround activity
473 requires a network with prominent recurrent *E-E* connectivity.
474
475 **Center activation lowers E/I balance of active SCs neurons in the surround**
476 Results obtained from the circuit mapping (Fig. 1) corroborated with the simulated network (Fig. 4)
477 indicate that the balance between excitation and inhibition (E/I) should shift to lower values in the
478 surround region when the center is stimulated (Fig. 5). To test this prediction, we intravitreally injected
479 wild-type C57BL/6NCrl mice with an AVV2-ChR2-EYFP (*N* = 5) to express ChR2 or an AAV2-mCherry
480 (*N* = 3, for control) in RGC axonal terminals (Fig. 5A-B). The successful activation of SCs neurons
481 following *in vivo* optostimulation of RGC terminals via an implanted fiber optic unilaterally was confirmed
482 through *cFos* labeling, a surrogate marker of neural activity (Fig. 5B-D). The animals were maintained
483 in a dark chamber to eliminate the potential influence of natural visually driven activity.
484
485 Figure 5B shows the distribution of active SCs cells in coronal sections (top is control, bottom is ChR2).
486 After control optostimulation, the presence of a sparse population of spontaneously active neurons
487 located could be seen reflecting baseline activity at approximate equidistant locations along the
488 mediolateral axis with a higher concentration near the midline (top image in Fig. 5B). Optostimulation of
489 ChR2-expressing RGC axonal terminals (bottom image in Fig. 5B; *see* Methods) revealed a significant
490 increase in *cFos* expression under the implant (top, Fig. 5C), with higher overall levels observed across
491 both hemispheres (bottom, Fig. 5C). Furthermore, during control the spatial distribution of active

neurons across the mediolateral axis maintained a balance across the hemispheres, which shifted in the case of ChR2-expressing RGC input activation (bottom, Fig. 5B).

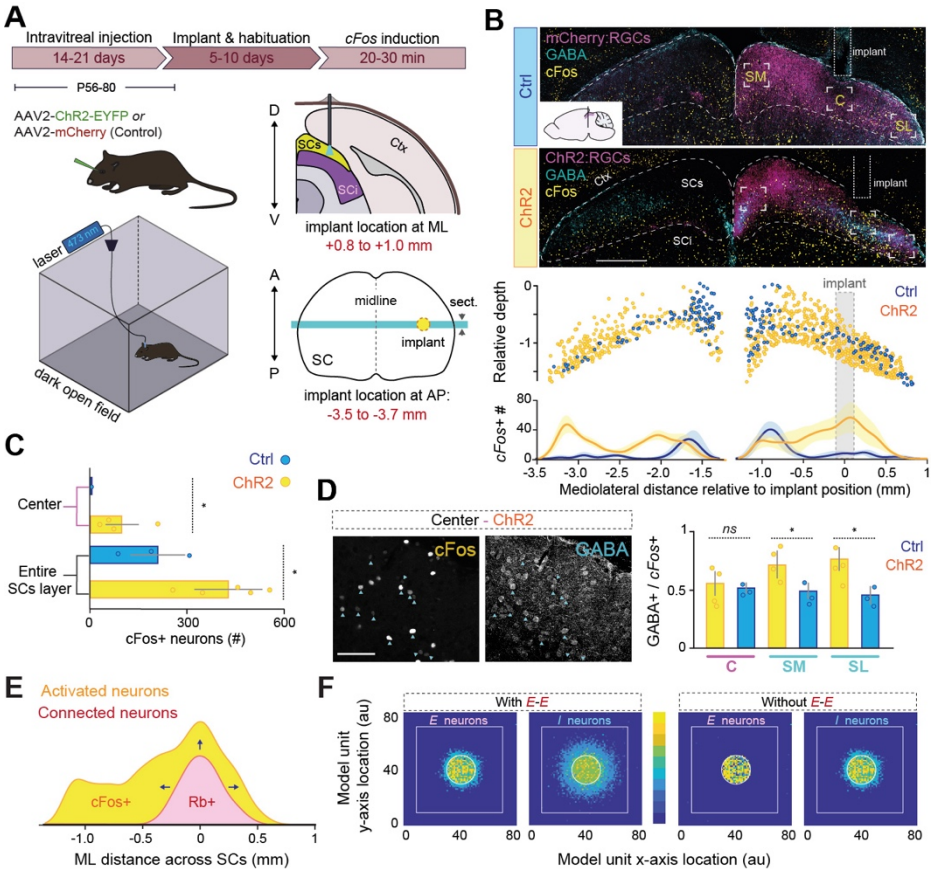

Fig. 5: Functional identification of active SCs neurons reveals that center activation lowers E/I balance in the surround

(A) Pipeline that we used to measure *in vivo cFos* expression induced by local optostimulation of RGC axonal terminals in the SCs. Top left: As in Fig. 1a, expression of ChR2 in RGCs was achieved using an intravitreal viral injection of the vector rAAV2-hsyn-hChR2(H134R)-EYFP (in WT mice, $N = 5$) or rAAV2-hsyn-mCherry for control (in WT mice, $N = 3$). Bottom left: schematic illustrating assay performed in a dark box. Right panels: cartoon of the optic fiber placement site shown in a coronal (top) and a horizontal (bottom) midbrain sections.
(B) Top panels: Coronal midbrain sections of the SCs centered around the implant for *cFos* induction following local optostimulation. Yellow, *cFos* immunostaining; magenta, control (top) or ChR2 (bottom); cyan, GABA immunostaining. Scale bar: 500 µm. *Abbrev*: C, center; SM (surround medial); SL (surround lateral). Bottom panels: The location (top) and distribution (bottom) of *cFos*+ neurons across the hemispheres of the SCs. Blue circles are control; Yellow circles are ChR2-induced. The central zone (C) is defined by the implant tip, which defines the origin of the x-axis. Shading is standard error.
(C) Comparison of the total cell count of *cFos*+ cells induced in SCs neurons between control (Ctrl, blue, $N = 3$) and during activation of ChR2-expressing RGC axonal terminals (ChR2, yellow, $N = 5$) across the entire SCs layer and center zone, respectively. Comparison of means performed using a *t*-test.
(D) Top: Grayscale image taken from the center region showing *cFos* (left) and GABA immunostaining (right). Blue arrows show colocalization. Bottom: Ratio of GABA+ to *cFos*+ cells across the three zones (C, SM and SL) compared between the two conditions (ChR2, $N = 4$; and Ctrl, $N = 3$). Statistical testing was done using *t*-test (*, $p < 0.05$; ***, $p < 0.0001$; *ns*, no significance). Bars show standard error of the mean.
(E) Comparison of the distribution between activated and connected neurons. Plot of activated neurons (in yellow) was obtained from the bottom right panel in **(B)**, whereas the plot of connected neurons (in red) was obtained using cell-type-specific trans-synaptic retrograde mapping shown in Fig. 1 and Fig. S1.

(F) Qualitative comparison of the effect with (left two panels) and without (right two panels) the recurrent *E-E* connection on the distribution of active neurons in response to center stimulation using the same model parameters used in Fig. 4. The square schematically shows the region in which neurons were placed on a square grid (as the bottom part of Fig. 4A). Inner circle is the site of center stimulation, whereas the surround is located between the inner white square excluding the area occupied by the white circle. Probability of spiking (estimated from 20 trials) of a neuron when center alone was stimulated. The color bar ranges from 0 to 1 and shows the probability of spiking when the center is stimulated.
Abbreviations: *C*, center; *SM*, surround medial; *SL*, surround lateral. *Ctx*, cortex, *Ctrl*, control.

Shifts in E/I balance were determined by quantifying the proportion of inhibitory neurons among the total activated cells. To do this, we defined the center region as the area located directly under the implant (C), along with two distal surround zones located more than 400 µm from the center: a medial surround zone (SM) and a lateral surround zone (SL). Figure 5D (top) shows a subset of *cFos* positive neurons in the center zone that were immunoreactive for the neurotransmitter GABA revealing their inhibitory origin (*see* also Supplementary Fig. S7). Notably, optostimulation drives a balance of excitation and inhibition in the center with a population of putative glutamatergic neurons (i.e., negative for GABA) that matches the population size of active inhibitory neurons (C: 0.49 ± 0.07, N = 4; mean ± s.e.m.). The fraction of colocalized neurons, however, shows a significant increase in the ratio of active GABAergic neurons in both surround zones compared to the center (SM: 0.70 ± 0.13, SL: 0.73 ± 0.14, N = 4; mean ± s.e.m.). This finding supports the notion that there will be fewer excitatory neurons active to amplify visual signals in the surround when the center is active, or vice versa, as demonstrated in the results presented in Fig. 3.

Figure 5E compares the spatial distribution between activated neurons (data from Fig. 5B) and connected neurons (data from Fig. 1H-I and Fig. S1E). Considering the unlikely event of activated fibers of passages targeting areas other than the center (*44*), which may contribute to this discrepancy, two plausible reasons can be identified: 1) activation of retinotopically-aligned recurrent networks and 2) activation of upstream circuits connected to the SCs arising, for example, from the V1 and parabigeminal nucleus (Fig. 5E). To explore whether local recurrent excitation can account for the observed drop in the surround E/I balance mediated, we tested the efficacy of the connectivity footprint by increasing the intensity of the model's center stimulation while utilizing the same parameters as depicted in Fig. 4 (*see* Table S5 for details). When recurrent excitatory connections were active (left two insets in Fig. 5F), center stimulation triggered neuronal activity in the surround, even in neurons outside the white circle representing the model 'center', as evidenced by the non-zero firing probability. This contrasts with the scenario without functional *E-E* connections (right two insets in Fig. 5F), where surround activity would be limited to a confined region. Recruited responses in inhibitory neurons spread out more than in excitatory neurons indicating the spatial discrepancy between the *E-E* and *E-I* connections, which we found to be independent of center size. This qualitative description obtained by the model simulation could explain shifts in surround E/I without the exclusive reliance on long-range horizontal connections.

Discussion

This study offers mechanistic insight into how the SCs generates recurrent-based center-surround interactions, capable of operating independently yet in parallel with cortical visual circuits. Targeted optogenetic activation of center and surround zones in individual neurons allowed us to test the presence and circuit implementation of surround modulation, using the SCs as a conserved model of early visual processing. Our experiments show that a selective decrease in center excitation occurs when the visual surround is active (Fig. 3); a potential computation contributing to midbrain target selection where a current central input becomes the next saccade's surround input. Given our experimental settings, this result proves that evoked changes in synaptic excitatory conductance of varying magnitude (usually moderate or strong) are due to local interactions placed within the midbrain SCs itself. This finding suggests that the main extraretinal circuits (i.e., SCs and V1) belonging to divergent subcortical and cortical pathways can perform surround suppression independently. This implies that a stimulus can undergo selective suppression in one pathway (e.g. thalamocortical) while concurrently being preferred in the other (e.g. retinotectal). Understanding how phylogenetically older and neocortical circuits can cooperate or compete is important for comprehending the versatility in pre-attentive visual processing.

As in cortical circuits (*45*), the SCs also contains excitatory and inhibitory neurons that are spatially intermingled, a feature that complicates the unravelling of their function. By combining connectivity analysis (Fig. 1), intracellular measurements (Fig. 2-3) and with a computational model (Fig. 4), we revealed two main local circuit motifs: recurrent excitation (*E-E*) and feedback inhibition (*I-E*) that contribute to surround suppression in distinct ways. *E-E* connections amplify responses in a specific retinotopic 'center' whereas *I-E* performs a dual function. It overlaps with center-specific *E-E*, thereby modulating the responses of the same center neurons subject to *E-E*, while simultaneously, reaching slightly beyond this zone, curbing the responsiveness of neighboring surround neurons outside the center (Fig. 1 and 4). In natural conditions, however, every input should be accompanied by some surround input since one neuron's center will be another neuron's surround. We show that in such a case, these recurrent interactions conspire to reduce the persistence of input in the absence of top-down input. Further research is required to establish whether multiple classes of inhibitory interneurons are involved in specific computations in the SCs, drawing parallels to findings in V1 where the potential role of somatostatin-positive (*46*) in coalition with recurrent excitatory connections (*47*) are involved in cortical surround suppression.

The question of whether these networks process all visual streams uniformly, with each stream conveyed by distinct RGC subtypes (of which more than 30 are known, *see* (*48*), can be addressed in future by using our approach presented in this study. For instance, some inputs may bypass this

circuitry, evade surround suppression, and avoid engaging *I-E* subcircuits. They may also selectively drive surround facilitatory connections for contour integration across the visual layer (*49*). These issues can be addressed by activating cell-type-specific RGC subtypes using opsins expressed in specialized Cre-lines, e.g., Kcng4-Cre for targeting alpha RGCs, *see* (*50*), instead of the pan-ganglion approach presented here. In essence, this study is designed to complement *in vivo* investigations by providing key insight into local circuit function. It underscores the importance of developing approaches that connect local processes to global network function, such as during surround interactions within motor or limbic systems, which present technical challenges *in vivo*.

Visual saliency computations in the SCs provide cortical circuits the flexibility to modulate SCs activity either by amplifying or suppressing with retinotopic correspondence (*see* white arrow in Fig. 1C, *see also* (*27*)). This could allow them to engage with SCs recurrent networks and modulate local center-surround dynamics in a top-down manner. For instance, by granting selective access for pyramidal neurons in V1 to interact with *E-E* connections, responses can be biased to specific incoming retinal inputs from certain areas of the visual field, or in contrast, they can be suppressed by activating *I-E* connections. Importantly, these phylogenetically conserved circuits in the SCs can also influence cortical activity via tecto-thalamic pathways (*51*), thereby influencing visual attention (*30*, *52*). This highlights the ability of SCs activity to modulate neural activity in both upstream and downstream targets, potentially influencing higher-order functions like visuospatial perception and behavioral selection.

In conclusion, our results show that selective decrease in center excitation when the visual surround is active is consistent with models that involve amplification in recurrent networks (*53*), but inconsistent with models that are dominated by feedback inhibition (*54*). In the latter, transient increase in inhibition would account for reduction in overall excitation and inhibition levels – an outcome that our measurements did not support. Computational models of trial-by-trial variability suggest that, while both increases in inhibition or decreases in recurrent excitation can similarly affect the average output response, the latter is more likely to minimize variability across trials (*55*). We propose that SCs circuitry has evolved to mitigate this variability where surround inputs are continuously transformed into center inputs during dynamic visual exploration.

Acknowledgements

We thank Drs. Michael Haüsser, Abdel El Manira and Julien Bouvier for comments on the manuscript. We thank Dr. Sten Grillner for his support throughout this study. We thank Drs. Mats Hellström and Sias Jordaan for technical assistance.

Funding

Swedish Research Council Starting Grant in Medicine no. 2016-03134 (AAK)
Swedish Research Council Project Grant in Medicine no. 2020-02927 (AAK)
CIDEGENT funding from the Valencian Community in Spain no. 2021-028 (AAK)
Strategic research area neuroscience (StratNeuro) Start-up program 2017 (AAK)
Swedish Brain Foundation Hjärnfonden no. FO2018-0254 (AAK)
Hedlunds Foundation no. M-2017-0691 (AAK)
Olle Engvist Foundation no. 196-0148 (AAK)
Stiftelsen Kronprinsessan Margeratas Arbetnämnd för synskadade no. 2019-027 and 2020-182 (AAK).

Author Contributions

PC performed electrophysiological recordings, viral injections, optogenetic experiments and data analysis. KS performed neuroanatomical experiments, RNAscope *in situ* hybridization, viral injections, fiber implantations and data analysis. DMM performed *in vivo cFos* induction experiments, visualization of neuroanatomy, and data analysis. AG. performed electrophysiological recordings. IL and TF contributed to neuroanatomy and *in vivo* experiments. AAK performed the conductance analysis. IL, KM, TF, and AAK contributed to the conceptualization and experimental study design. KM contributed vectors and resources for visualization of neuroanatomical data. AK contributed to the computational study design and performed the numerical experiments. AAK designed the figures, supervised and funded the study. AAK wrote the manuscript with help from AK All authors reviewed and commented on the manuscript.

Material and Methods

Animal strains

Experimental procedures were approved by the Stockholm municipal committee for animal experiments and the Karolinska Institute in Sweden (N9179-2017 and N6747-2019 to A.A.K.), as well as, the Committee on Animal Research at the Universidad Miguel Hernández and carried out in compliance with the Research Council of Spain (CSIC), the Generalitat Valenciana (GVA) and European regulations (2022/VSC/PEA/0236 to A.A.K.). Both male and female vGAT-Cre (Jackson: Slc32a1tm2(cre)Lowl), vGluT2-Cre (Jackson: Slc17a6tm2(cre)Lowl) and wild-type mice (C57BL/6N; Charles River) were used throughout the experiments. Mice were kept on a 12-h day/night cycle under stable temperature (21 ± 1 °C) and air humidity (50–65%) with freely available food and water. The exact numbers of cells (*n*) and animals (*N*) used for each experiment are reported in the *Results* section and corresponding figure legend.

669
670 **Viral injections**

671 The complete list of viruses we used is provided in Supplementary Table 1. Injections were performed
672 in 2–5 months old wild-type mice and transgenic mice under isoflurane anesthesia and injected with
673 buprenorphine post-surgery. Viral titers of adeno-associated viruses (AAV) and modified rabies virus
674 were between 1×10^{12} and 1×10^{13} viral genomes per milliliter (vg/mL). To express ChR2 in the axons
675 of RGCs in the superficial layer of the right hemisphere SC, we injected 1000 nL into the vitreous bodies
676 of the left retinas using the following viral vectors:

677 1. rAAV2/hsyn-hChR2(H134R)-EYFP-WPRE-PA (UNC Vector Core),

678 2. rAAV2/hsyn-hChR2(H134R)-mcherry-WPRE-PA (UNC Vector Core),

679 3. rAAV2-EF1α-DIO-hChR2(H134R)-EYFP (UNC Vector Core), or

680 4. ssAAV-2/2-shortCAG-dlox-hChR2(H134R)_EYFP(rev)-dlox-WPRE-hGHp(A) (VVF, Zurich).

681 We used the vector rAAV2/hsyn-mcherry (UNC Vector Core) as in our control group for the intravitreal
682 injections. To identify GABAergic neurons in the SCs, the vector rAAV5-CAG-FLEX-tdTomato (400 nL,
683 UNC Vector Core) was injected into two collicular sites in order to maximize expression: 1) the rostral
684 SCs (from bregma: anteroposterior (AP) -3.6 mm; right (R) -0.8 mm; dorsoventral (DV) -1.6 mm from
685 the surface of the skull), and 2) the caudal SCs (AP -4.2 mm; R -1.8 mm; DV -1.5 mm) respectively on
686 the same day.

687 For the rabies virus tracing, 50 nL of helper virus AAV5-EF1a-DIO-TVA-V5-t2A-RG was injected into
688 the right SCs (AP -3.9 mm; R -0.8 mm; DV -1.05 to -1.15 mm from the surface of the brain) in vGAT-
689 Cre or vGluT2-Cre mice, while taking great care to maintain viral spread to within the SCs layer. Three
690 weeks later, 150 nL of the engineered rabies virus EnvA-coated G-deleted rabies virus with EGFP
691 (EnvA-ΔG-Rb-EGFP) was injected into the same location.

692

693 For secondary injections, fiber optic implantations and electrophysiological recordings, two to three
694 weeks were allowed to pass after the initial injection. Viral suspensions were delivered at 500 nL/min
695 and 100 nL/min for intravitreal and brain injections, respectively. A puncture was made 2 mm posterior
696 to the corneal limbus using a sterile 30-gauge (G) needle after pupil dilation was achieved with 0.5%
697 Alcaine. After which 1000 nL vitreous was aspirated manually using a Hamilton microliter syringe. The
698 glass capillary was then inserted through the same puncture by using a microliter syringe (1.5 mm
699 volume) into the eye, and the tip was angled toward the vitreous humor and back of the eye, taking
700 care to avoid any damage to the retina or lens. The capillary remained in the eye for 2 min in order to
701 prevent reflux of the viral suspensions. Brain injections were performed by using a digital stereotaxic

702 frame combined with a Quintessential Stereotaxic injector (Stoelting) via a glass capillary. The capillary
703 firstly reached 0.2 mm deeper than the target location to give space for the viral suspensions, then was
704 slowly retracted to the target location to complete the injections. Afterwards, the capillary was retracted
705 by 0.2 mm again and remained in position for 8 min. During the injections, all the mice were kept on a
706 heating pad at 37 °C with a subcutaneous injection of buprenorphine while maintaining the eyes were
707 moisturized with Viscotears gel.

708 **Patch electrophysiology in acute midbrain slices**

709 The animals were deeply anaesthetized by using a combination of pentobarbital injected
710 intraperitoneally. To ensure rapid cooling of the midbrain, we perfused the animals transcardially with
711 an ice-cold cutting solution, containing the following (in mM): NaCl 40, KCl 2.5, NaH_2PO_4 1.25, $NaHCO_3$
712 26, glucose 20, sucrose 37.5, HEPES 20, NMDG 46.5, Na L-ascorbic acid 5, $CaCl_2$ 0.5 and $MgCl_2$ 5
713 (pH 7.3 with HCl). The brain was rapidly dissected out after decapitation. Coronal midbrain slices (400
714 µm) were prepared by using a vibratome (VT1000S, Leica, Germany) in the cutting solution and
715 incubated in the same solution at 35 °C for 12 min. Slice orientation was chosen to profile responses
716 along the medio-lateral axis corresponding to the spatial axis of the retina across the dorso-ventral
717 direction of visual space, whereas the dorsal-ventral axis of the SCs slice corresponded to the various
718 sublaminae of the SCs. The sections were subsequently maintained at room temperature in recording
719 solution that contained the following (in mM): NaCl 124, KCl 2.5, NaH_2PO_4 1.25, $NaHCO_3$ 26, glucose
720 20, $CaCl_2$ 2 and $MgCl_2$ 1 (pH 7.3). Cutting and recording solutions were continuously infused with
721 carbogen (95% O_2 and 5% CO_2) throughout the procedure.

722 Whole-cell patch clamp recordings were either performed on random neurons in the SCs of wild-type
723 mice or tdTomato-expressing neurons of vGAT-Cre mice at room temperature using pCLAMP 11
724 (Molecular Devices, USA). Midbrain slices were continuously perfused with oxygenated recording
725 solution at a rate of 2 mL/min during recording and visualized under an upright CleverScope motorized
726 microscope (Micro Control Instruments, UK) equipped with a Dodt gradient contrast system (DGC-2),
727 an oil condenser (U-AAC, Olympus, Japan) and two Chameleon3 cameras (Teledyne FLIR, USA).
728 Whole-cell recordings were obtained under visual control using a 16× (0.80 NA) water dipping objective
729 (CFI75 LWD 16X W, Nikon, Japan) combined with 2× c-mount extender (EX2C, Computar, USA) and
730 c-mount adapters (U-TV1X-2 and U-CMAD3, Olympus, Japan) with Axon MultiClamp 700B amplifier
731 and Axon Digidata 1320A digitizer (Molecular Devices, USA). Signals were sampled at 20 kHz. Pipettes
732 used for recording were pulled from borosilicate glass capillaries (article no. 1403542, Hilgenberg,
733 Germany) by a P-97 Micropipette Puller (Sutter Instrument, USA). Patch pipettes (5–8 MΩ) were filled
734 with a potassium gluconate based intracellular solution contained (in mM): K D-gluconate 125, EGTA
735 1, KCl 10, HEPES 10, ATP-Mg 4, GTP-Na 0.3, phosphocreatine 10, $CaCl_2$ 0.1 and QX314 3 (pH 7.2
736 with KOH; 290 mOsm). Due to the long recording times (usually one hour), the access resistance was

evaluated every 10 min to ensure that initial values (only under ~30 MΩ were considered) did not increase throughout the recording session.

ChR2-expressing axons of retinal ganglion cells were optically stimulated with 470 nm light from a high-power collimated LED source (Mightex, Canada) connected to a digital mirror device (Polygon1000, Mightex, Canada) by a 3 mm-core liquid lightguide (Newport, USA). The stimulation patterns were triggered via Master-8 pulse stimulator (A.M.P.I, Israel) and designed via the software PolyScan2 (Mightex, Canada). TdTomato-expressing vGAT-positive neurons in the SCs were detected with 540 nm light from a high-power collimated LED source (Mightex, Canada) and an RFP filter set (Olympus, Japan). The 540 nm LED was connected to a 495 nm dichroic filter cube (Mightex, Canada) with the 470 nm LED during the transgenic animal experiments. Both LEDs were directed via a four channel BioLED light source control module (Mightex, Canada).

For membrane property measurements, a series of 1000 ms negative and positive injected current steps from -30 pA to +40 pA in 5 pA increments were delivered through the recording electrode under current-clamped conditions to each recorded neuron.

Functional receptive field mapping of individual neurons

We combined whole-cell electrophysiology with a digital mirror device (DMD) based dual camera system to map the receptive fields of individual neurons. Optogenetic stimulation patterns were created and performed during the recordings by the DMD (Polygon1000, Mightex, Canada). The 16× objective combined with the 2× front tube optics (Mightex, Canada) and 0.5× single photo port tube lens camera adapter (Olympus, Japan) enabled a large workable field-of-view (~1.2 × 1 mm working area). With this customized visual inspection system with this dual camera approach, whole-cell patch-clamp recordings were performed using the high magnification light pathway whereas optostimulations patterns could be performed using the low magnification pathway that enables the large field of view. All neurons were voltage-clamped to −65 and 0 mV to measure excitatory postsynaptic currents (EPSCs) and inhibitory postsynaptic currents (IPSCs) respectively, while an intermediate potential (-45 mV) was also applied for membrane potential recordings in most neurons when the recordings were sufficiently stable.

For control experiments, whole-field stimulation patterns were delivered by 10 Hz trains of 8 stimuli (5 ms duration), followed by a single test stimulus at 5 s time interval, and each trace included four repetitive sweeps. For the center-surround experiments, SCs neurons were subjected to the following patterns: 'GridScan', 'Center-Center', 'Surround-Surround' and 'Surround-Center'. Center (C) and Surround (S) areas were determined by using the GridScan protocol, which was delivered 10 Hz trains of 5 light pulses of 5 ms duration in 100 non-adjacent grids arranged in a 10 × 10 spatial configuration

772 across the FOV (0.1 × 0.07 mm for each one). After the end of the GridScan, we promptly calculated
773 the maximum EPSC and IPSC amplitudes for each grid after it was normalized and filtered using
774 custom-written MATLAB (MathWorks). Excitatory postsynaptic current amplitudes arising from each grid
775 location were thresholded on the basis of their evoked amplitude. Grid locations that yielded ≥ 10-20%
776 of the peak EPSC amplitude for the recorded neuron, were considered to be part of the center zone,
777 whereas locations that did not pass this threshold were considered to be part of the surround zone. To
778 trigger center-surround interactions, the surround was optostimulated by a single pulse that was then
779 followed by a two or five-pulse train stimulation delivered to the center. We experimented with a range
780 of different surround stimulation durations (5, 20, 50 ms) and with a range of surround-center delays (0,
781 10, 20, 50 ms) to explore the parameter space. The inter-trial interval was 25 ± 5 s.
782

783 **Drugs used in electrophysiology**

784 Drugs were bath applied and an overall duration of at least 5 min was allowed before testing their effects,
785 which was followed by a washout phase of at least 10 minutes. Unless otherwise indicated, drugs were
786 perfused during patch-clamp recordings under the given conditions using a two-gauge peristaltic pump
787 (Pretech Instruments, Sweden). The complete list of drugs used is provided in Supplementary Table 2.
788

789 **Estimation of synaptic conductances**

790 To deconvolve inhibitory and excitatory synaptic conductance, recordings were performed during
791 'center-center', 'surround-surround', 'surround-center', and 'global' optostimulation. A QX314-based
792 intracellular solution was used in the recording pipette to improve intrinsic conductance isolation and
793 block action potential discharge conditions (Fig. 2-3 and Fig. S2-3). Evoked synaptic currents used in
794 this analysis were obtained by averaging values from 5 to 10 sweeps for each recorded cell. Due to the
795 long recording times (usually one hour), the access resistance was evaluated every 10 min to ensure
796 that initial values (only < ~30 MΩ were considered) did not increase throughout the recording session
797 at each membrane potential. Customized MATLAB scripts were written to estimate the total, excitatory
798 and inhibitory synaptic conductances based on the equations used in (*40*, *41*).
799

800 **Neuronal reconstruction**

801 To identify the dendritic fields from the recorded neurons, we used 0.3% Neurobiotin (Vector
802 Laboratories, no. VESP-1120-50) in the intracellular solution during whole-cell recordings. We post
803 fixed the midbrain slices and then used PBS to wash them. To visualize the neurons, we stained them
804 with streptavidin Cy5 (1:400, Jackson ImmunoResearch, no. 016-170-084) and imaged them using
805 confocal microscopy with a 20× objective (LSM-800, Zeiss, Germany). The images were processed
806 with ImageJ software, and the neurons were reconstructed by using the plugin Simple Neurite tracer.
807 The dendritic areas of each labeled neuron were calculated by tracing a convex polygon around the

808 outermost tips of the dendritic field. The SC cell types were then classified on the basis of their geometry
809 (*42*).

810

811 **Fiber optic implantation and cFos activation**

812 Two weeks after the intravitreal injection, a 200 μm diameter fiber optic (Thorlabs, FG200UEA) was
813 implanted into the right SCs (from bregma: AP -3.6 mm; R -1.0 mm; DV -1.0 mm from the brain surface).
814 The mice recovered for at least one week before the cFos induction experiment. The mice were
815 habituated to handling in an open field area (60 cm × 60 cm × 60 cm; W×D×H) and the connected optic
816 fiber for at least 3 days before proceeding with the experiment. To minimize stress, bedding from the
817 cage was placed in the box. Optogenetic stimulation was not initiated for 90 min after the mice were
818 placed in the dark box to avoid any prior visual effects on the observed cFos expression. The RGC
819 axonal terminals in the SCs were stimulated with a train of 1 s square pulses of 40 Hz frequency (10
820 ms ON and 15 ms OFF) every 10 sec for a total of 40 min. After the stimulation period, the mice were
821 left undisturbed for 60-70 min to ensure sufficient cFos protein expression. A maximum of 90 min after
822 the end of the stimulation period was allowed before the mice were euthanized with pentobarbital and
823 perfused with ice-cold 4% paraformaldehyde (PFA) in 0.01 M (1×) phosphate-buffered saline (PBS)
824 buffer. The brain and retinas were subsequently dissected, and post fixed in 4% PFA overnight at 4°C.

825

826 **Immunofluorescent staining and *in situ* hybridization**

827 Mice were anesthetized by pentobarbital and perfused with 1× PBS and 4% PFA. The brains (and
828 eyes, to confirm pan-retina transfection) were harvested and fixed in PFA at 4 °C overnight, then
829 washed with PBS for 3 times. The brain was placed in 15% sucrose solution for 24 h, then transferred
830 into 30% sucrose solution for 24–72 h. The brains were subsequently embedded in optimal cutting
831 temperature compound (OCT), frozen with dry ice and kept at -20 °C for short-term storage. The
832 cryostat sectioning was performed on a Epredia NX70 cryostat. The brains, between the thalamus and
833 brainstem, were sectioned in 14 μm thickness, about 80% (12 to 15) sections in the SCs were collected
834 on glass slides, and every 6th section was sampled for the following staining (the interval is about 0.105
835 mm). The other parts of the brain were sectioned in 40 μm thickness and stored in 1× PBS with 0.01%
836 sodium azide.

837 The fluorescence *in situ* hybridization was performed with RNAscope Multiplex Fluorescent Reagent
838 Kit v2 (ACD, Cat. No. 323100). The probes for vGluT2 (Mm-Slc17a6-C2, ACD, Cat. No. 319171-C2)
839 and vGAT (Mm-Slc32a1, ACD, Cat. No. 319191) were used to identify the cell types. The
840 manufacturer's protocol was followed. Co-staining of vGAT and vGluT2 *in situ* hybridizations was also
841 performed for control experiment, and the results were shown in Fig. S1.

Immediately following the *in situ* hybridization, the brain sections were incubated in chicken anti-V5 primary antibody (Abcam, ab9113) in 1:750 at room temperature overnight, then washed with 1× TBST (0.3% TritonX-100), and incubated in donkey anti-chicken Cy3 secondary antibody (Jackson ImmunoResearch, no. 703-165-155) in 1:1000. All the antibodies were diluted with 1× TBST (0.3% TritonX-100, 3% BSA, 0.01% sodium azide). After PBS washing and DAPI staining, the sections were mounted with an antifade mounting medium (VWR, BSBT AR1109). For the cFos staining, rat or rabbit anti-cFos primary antibodies (Synaptic Systems, no. 226-017 or no. 226-003, 1:500) and GABA primary antibody (Sigma-Aldrich, A2052, 1:2000) were used in 1× PBST (0.3% TritonX-100, 5% donkey serum, 0.01% sodium azide) at room temperature overnight, then the sections were stained with Cy3 donkey anti-rabbit (Jackson ImmunoResearch, no. 711-165-152) or AF647 donkey anti-rat (Jackson ImmunoResearch, no. 712-605-153). The same following steps are previously described.

The retinas were first removed from the eye in the perfused animals and then flattened with the help of four incisions, and finally washed in 1x PBS for 3 times. For the retina immunostaining, the retina was first treated with pre-heated (about 70 °C) 1× antigen retrieval citrate buffer (Sigma, C9999), then followed the same protocol as with the brain section described above. Rabbit anti-S-opsin primary antibody (Sigma, AB5407) and donkey anti-rabbit Cy3 secondary antibody were both used in 1:1000 to visualize the short-wave photoreceptors, which reveals retinal orientation.

Network model

We used an integrate and fire model to simulate the dynamics of neurons. The subthreshold membrane potential (V_m) of each neurons was described by the following differential equation:

$$C_m dV_m/dt = g_L (V_m - E_L) + I^{bkg}_{syn} + I^{net}_{syn} + I^{stim}_{syn},$$

where C_m is the membrane capacitance, g_L is the leak conductance, I^{net}_{syn} is the total synaptic input from neurons within the network, I^{bkg}_{syn} is the background input from other networks, I^{stim}_{syn} is input corresponding to center or surround inputs (*see* Supplementary Table S3). When the membrane potential reached V_{th}, spike was elicited and the V_m was reset to E_L for t_{ref} millisecond. In the network all neurons were identical. Neuron parameters are provided in Table S4.

Synaptic inputs were modelled as conductance transients with following dynamics:

$$g_{syn} = J_{syn} t/tau_{syn} \exp(-(t-(t_{spk}+ d_{syn}))/tau) \text{ when } t-t_{spk} >0 \text{ else } g_{syn} = 0,$$

where t_{spk} is the spike time, d_{syn} is the synaptic delay, J_{syn} *{syn: ee, ei, ie, ii, ex, ix)* is the amplitude of the postsynaptic potential (PSP), and tau_{syn} is the synaptic time constant. In our model all synapses of a particular type (external, excitatory, or inhibitory) have the same parameters (*see* Supplementary

Table S5). In our model we fixed the amplitude (J_{syn}) of the external excitatory (J_{ex}), inhibitory (J_{ix}) synapses and J_{ii} (inh. → inh.). The value of J_{ee} (exc. → exc.), J_{ei} (exc. → inh.), and J_{ie} (inh. → exc.) were systematically varied. Synapse parameters are provided in Table S5.

We considered a network with 6400 excitatory and 6400 inhibitory neurons. Neurons were placed on an 80 × 80 grid. Because we have the same population size for the two neuron types, both types of neurons were placed on the same size grid. Neurons were connected based on their spatial distance. To avoid boundary effects, the 80 × 80 grid was folded as a torus. The connection probability decreased as a function of distance according to a Gaussian function. The standard deviation of the Gaussian was set to 16 and 20 for excitatory and inhibitory synapses, respectively. This was based on our experimental data which showed that inhibitory neurons have a slightly broader extent of their spatial connectivity than that of excitatory synapses (Fig. 1 and Fig. S1). 16 and 20 grid points constitute 2% and 2.5% of our network space. The area of the Gaussian function (*i.e.* the total number of connections sent out by a neuron) was decided based on the input convergence we measured in our experiments (Fig. H-I). Network connectivity parameters are provided in Table S6.

Each neuron received Poisson type excitatory and inhibitory spiking inputs to mimic inputs from outside the network and to obtain a low firing rate (< 1 Hz) background activity. *See* Supplementary Table S7 for parameters.

To model a short flash like input to the center region, we selected 314 excitatory and 314 inhibitory neurons, located in a circle (radius = 10 grid points) at the center of our network model. These neurons received a single synchronous spike from 10 presynaptic neurons (from the retina). Each spike elicited 1.1 mV depolarization. Each neuron received such a synchronous spike event at the stimulus onset (*Tcenter*). Each individual neuron received the synchronous spike event at a time *Tcenter* + *r,* where *r* is a random number drawn from a uniform distribution (U[0,1]). Center stimulus was presented to the neurons in three conditions: center only, center stimulus just at the end of the surround stimulus (*see* below) and center while the surround stimulus was still on. *See* Supplementary Table S3 for more details.

To mimic the surround stimulus, we selected 3286 E-neurons and 3286 I-neurons from a square region in the network with a side of 60 grid points. The center neurons (see above) were located at the center of this square. For the surround stimulus we excluded the center neurons. The surround stimulus was injected in the selected neurons in the form of uncorrelated Poisson type spike trains. See Supplementary Table S3 for more details.

The network model was simulated using the simulator NEST(*56*).

909 **Statistical analysis and data plotting**

910 For each mouse, 10–16 sections were stained and visualized. Confocal images (20×) were used for the
911 manual scoring of co-expression of vGAT/vGluT2, V5 and RV-GFP. Whole-brain images (10×) were
912 acquired with a fluorescent microscope (Leica DM6000B) and a digital camera (Hamamatsu Orca-
913 FLASH 4.0 C11440). They were manually registered to a bregma AP coordinate (from bregma -3.2 to -
914 4.9), and subsequently aligned to the Allen Reference Atlas with the WholeBrain R package (*34*, *57*).
915 Every detected Rb-EGFP positive neuron was registered, and the coordinates were used for the
916 following analysis. As the main source of monosynaptic input and local input, only the RV-GFP positive
917 cells in the SCs were included in the calculation. For the comparison between mice, the number of input
918 neurons were normalized to the total number of detected Rb-EGFP positive neurons in SCs. All the
919 density estimations were done using a Gaussian kernel and were then plotted in R.

920 To minimize the effects of M-L differences of the injection sites between animals, the centroid of the
921 starter neurons was first computed using k-means clustering analysis, which then allowed us to plot
922 the relative M-L coordinate for each neuron. As for the depth estimation, the coordinates of the SC
923 surface were first obtained with the WholeBrain R package, then the depth of each neuron was
924 calculated after subtracting the difference. In both, M-L and depth density plots, only 3 central brain
925 sections with the highest starter density were included according to the AP density plot.

926

927 After confocal imaging the *cFos* fluorescence was quantified by a 3d object counter plug-in of Fiji.
928 Colocalized *cFos*+ and GABA+ cells were manually counted in three areas in SCs (C, SM and SL; *see*
929 Fig. 5). The statistical analysis and visualization were done in Python (code available upon request).

930

931 We used three model stimulation protocols: center only (center), center stimulus just at the end of the
932 surround stimulus (center after surround) and center while the surround stimulus was still on (center
933 with surround). Each paradigm was repeated 20 times. For each stimulus presentation, we recorded
934 excitatory conductance from a single neuron. We estimated the across trial mean and variance of the
935 conductance input to the recorded neuron. Finally, the results were rendered as the mean and variance
936 of the excitatory conductance at specific time points after the onset of the stimulus in all three stimulus
937 paradigms. In addition, we recorded spiking activity from all the neurons and estimated the firing rate
938 of neurons. The network model was simulated using the simulator NEST. All differential equations were
939 integrated using Runga-Kutta method with a time step of 0.1 ms.

940

Electrophysiology data analyses were performed using Clampfit 11 (Molecular Devices, USA), GraphPad Prism (GraphPad Software 7.00, USA), ImageJ (1.53c, NIH, USA), RStudio (R 3.6.1) or MATLAB (R2018b, MathWorks, USA). Data were all presented as mean values ± s.e.m. Before performing paired *t*-test or one-way ANOVA analysis, the normality and the homogeneity of variance were first evaluated using Kolmogorov–Smirnov's test and Brown–Forsythe's test. If the *p* value of Kolmogorov–Smirnov's test was less than 0.05, Wilcoxon's signed-rank test would be used instead of paired *t*-test. If *p* value of Brown–Forsythe's test was less than 0.05, Friedman test and Kruskal–Wallis test would be used instead of a repeated-measures one-way ANOVA (RM one-way ANOVA) and ordinary one-way ANOVA, respectively. *p* values were corrected for deviation using the Geisser–Greenhouse correction. Once the *p* value of a one-way ANOVA analysis was less than 0.05, Tukey's multiple comparisons test would be performed. *F* and df (df1, df2) are degrees of freedom for one-way ANOVA and paired *t*-test, respectively. *p* values less than 0.05 were considered significant with asterisks in figures denoting as follows: $*p < 0.05$, $**p < 0.01$, $***P < 0.001$, $****p < 0.0001$, *ns*, no significance. Traces showing electrophysiological recordings plotted in the figures were not corrected for the liquid junction potential, which was experimentally found to be -9.8 mV (~-10 mV). It was taken, however, into consideration when estimating for their underlying evoked synaptic conductance.

REFERENCES

1. P. S. Churchland, T. J. Sejnowski, Neural Representation and Neural Computation. *Philos. Perspect.* **4**, 343–382 (1990).

2. S. Grossberg, The quantized geometry of visual space: The coherent computation of depth, form, and lightness. *Behav. Brain Sci.* **6**, 625–657 (1983).

3. A. Angelucci, M. Bijanzadeh, L. Nurminen, F. Federer, S. Merlin, P. C. Bressloff, Circuits and Mechanisms for Surround Modulation in Visual Cortex. *Annu. Rev. Neurosci.* **40**, 425–451 (2017).

4. E. I. Knudsen, M. Konishi, Center-Surround Organization of Auditory Receptive Fields in the Owl. *Science* **202**, 778–780 (1978).

5. R. Sachdev, M. Krause, J. Mazer, Surround suppression and sparse coding in visual and barrel cortices. *Front. Neural Circuits* **6** (2012).

6. S. R. Olsen, R. I. Wilson, Lateral presynaptic inhibition mediates gain control in an olfactory circuit. *Nature* **452**, 956–960 (2008).

7. D. H. Hubel, T. N. Wiesel, Receptive fields of single neurones in the cat's striate cortex. *J. Physiol.* **148**, 574–591 (1959).

8. P. H. Schiller, F. Koerner, Discharge characteristics of single units in superior colliculus of the alert rhesus monkey. *J. Neurophysiol.* **34**, 920–936 (1971).

9. A. A. Kardamakis, K. Saitoh, S. Grillner, Tectal microcircuit generating visual selection commands on gaze-controlling neurons. *Proc. Natl. Acad. Sci.* **112**, E1956–E1965 (2015).

10. M. Kasai, T. Isa, Imaging population dynamics of surround suppression in the superior colliculus. *Eur. J. Neurosci.* **44**, 2543–2556 (2016).

11. J. T. McIlwain, P. Buser, Receptive fields of single cells in the cat's superior colliculus. *Exp. Brain Res.* **5**, 314–325 (1968).

12. P. H. Schiller, M. Stryker, Single-unit recording and stimulation in superior colliculus of the alert rhesus monkey. *J. Neurophysiol.* **35**, 915–924 (1972).

13. V. Bonin, V. Mante, M. Carandini, The Suppressive Field of Neurons in Lateral Geniculate Nucleus. *J. Neurosci.* **25**, 10844–10856 (2005).

14. H. E. Jones, K. L. Grieve, W. Wang, A. M. Sillito, Surround suppression in primate V1. *J. Neurophysiol.* **86**, 2011–2028 (2001).

15. R. T. Born, D. C. Bradley, Structure and Function of Visual Area Mt. *Annu. Rev. Neurosci.* **28**, 157–189 (2005).

16. A. M. Fernandes, D. S. Mearns, J. C. Donovan, J. Larsch, T. O. Helmbrecht, Y. Kölsch, E. Laurell, K. Kawakami, M. dal Maschio, H. Baier, Neural circuitry for stimulus selection in the zebrafish visual system. *Neuron* **109**, 805-822.e6 (2021).

17. A. A. Kardamakis, J. Pérez-Fernández, S. Grillner, Spatiotemporal interplay between multisensory excitation and recruited inhibition in the lamprey optic tectum. *eLife* **5**, e16472 (2016).

18. N. Flores-Herr, D. A. Protti, H. Wässle, Synaptic currents generating the inhibitory surround of ganglion cells in the mammalian retina. *J. Neurosci. Off. J. Soc. Neurosci.* **21**, 4852–4863 (2001).

19. Y. J. Kim, B. B. Peterson, J. D. Crook, H. R. Joo, J. Wu, C. Puller, F. R. Robinson, P. D. Gamlin, K.-W. Yau, F. Viana, J. B. Troy, R. G. Smith, O. S. Packer, P. B. Detwiler, D. M. Dacey, Origins of direction selectivity in the primate retina. *Nat. Commun.* **13**, 2862 (2022).

20. S. G. Solomon, B. B. Lee, H. Sun, Suppressive Surrounds and Contrast Gain in Magnocellular-Pathway Retinal Ganglion Cells of Macaque. *J. Neurosci.* **26**, 8715–8726 (2006).

21. Y. Zhang, I.-J. Kim, J. R. Sanes, M. Meister, The most numerous ganglion cell type of the mouse retina is a selective feature detector. *Proc. Natl. Acad. Sci.* **109**, E2391–E2398 (2012).

22. M. Carandini, D. J. Heeger, Normalization as a canonical neural computation. *Nat. Rev. Neurosci.* **13**, 51–62 (2012).

23. T. K. Sato, B. Haider, M. Häusser, M. Carandini, An excitatory basis for divisive normalization in visual cortex. *Nat. Neurosci.* **19**, 568–570 (2016).

24. X. Zhang, L. Zhaoping, T. Zhou, F. Fang, Neural Activities in V1 Create a Bottom-Up Saliency Map. *Neuron* **73**, 183–192 (2012).

25. L. Zhaoping, From the optic tectum to the primary visual cortex: migration through evolution of the saliency map for exogenous attentional guidance. *Curr. Opin. Neurobiol.* **40**, 94–102 (2016).

26. R. Veale, Z. M. Hafed, M. Yoshida, How is visual salience computed in the brain? Insights from behaviour, neurobiology and modelling. *Philos. Trans. R. Soc. B Biol. Sci.* **372**, 20160113 (2017).

27. M. Ahmadlou, A. Tafreshiha, J. A. Heimel, Visual Cortex Limits Pop-Out in the Superior Colliculus of Awake Mice. *Cereb. Cortex* **27**, 5772–5783 (2017).

1017 28. R. M. McPeek, E. L. Keller, Deficits in saccade target selection after inactivation of superior
1018 colliculus. *Nat. Neurosci.* **7**, 757–763 (2004).

1019 29. L. Wang, J. P. Herman, R. J. Krauzlis, Neuronal modulation in the mouse superior colliculus
1020 during covert visual selective attention. *Sci. Rep.* **12**, 2482 (2022).

1021 30. L. Wang, R. J. Krauzlis, Visual Selective Attention in Mice. *Curr. Biol.* **28**, 676-685.e4 (2018).

1022 31. H. Ozeki, I. M. Finn, E. S. Schaffer, K. D. Miller, D. Ferster, Inhibitory Stabilization of the Cortical
1023 Network Underlies Visual Surround Suppression. *Neuron* **62**, 578–592 (2009).

1024 32. D. B. Rubin, S. D. Van Hooser, K. D. Miller, The Stabilized Supralinear Network: A Unifying Circuit
1025 Motif Underlying Multi-Input Integration in Sensory Cortex. *Neuron* **85**, 402–417 (2015).

1026 33. Y. Liu, E. L. Savier, V. J. DePiero, C. Chen, D. C. Schwalbe, R.-J. Abraham-Fan, H. Chen, J. N.
1027 Campbell, J. Cang, Mapping visual functions onto molecular cell types in the mouse superior
1028 colliculus. *Neuron* **111**, 1876-1886.e5 (2023).

1029 34. S. Ährlund-Richter, Y. Xuan, J. A. van Lunteren, H. Kim, C. Ortiz, I. Pollak Dorocic, K. Meletis, M.
1030 Carlén, A whole-brain atlas of monosynaptic input targeting four different cell types in the medial
1031 prefrontal cortex of the mouse. *Nat. Neurosci.* **22**, 657–668 (2019).

1032 35. I. Lazaridis, O. Tzortzi, M. Weglage, A. Märtin, Y. Xuan, M. Parent, Y. Johansson, J. Fuzik, D.
1033 Fürth, L. E. Fenno, C. Ramakrishnan, G. Silberberg, K. Deisseroth, M. Carlén, K. Meletis, A
1034 hypothalamus-habenula circuit controls aversion. *Mol. Psychiatry* **24**, 1351–1368 (2019).

1035 36. I. R. Wickersham, D. C. Lyon, R. J. O. Barnard, T. Mori, S. Finke, K.-K. Conzelmann, J. A. T.
1036 Young, E. M. Callaway, Monosynaptic restriction of transsynaptic tracing from single, genetically
1037 targeted neurons. *Neuron* **53**, 639–647 (2007).

1038 37. K. Reinhard, C. Li, Q. Do, E. G. Burke, S. Heynderickx, K. Farrow, A projection specific logic to
1039 sampling visual inputs in mouse superior colliculus. *eLife* **8**, e50697 (2019).

1040 38. T. McLaughlin, D. D. M. O'Leary, Molecular gradients and development of retinotopic maps. *Annu.*
1041 *Rev. Neurosci.* **28**, 327–355 (2005).

1042 39. P. Phongphanphanee, R. A. Marino, K. Kaneda, Y. Yanagawa, D. P. Munoz, T. Isa, Distinct local
1043 circuit properties of the superficial and intermediate layers of the rodent superior colliculus. *Eur.*
1044 *J. Neurosci.* **40**, 2329–2343 (2014).

1045 40. B. Haider, M. Häusser, M. Carandini, Inhibition dominates sensory responses in the awake cortex.
1046 *Nature* **493**, 97–100 (2013).

1047 41. M. Wehr, A. M. Zador, Balanced inhibition underlies tuning and sharpens spike timing in auditory
1048 cortex. *Nature* **426**, 442–446 (2003).

1049 42. S. D. Gale, G. J. Murphy, Distinct Representation and Distribution of Visual Information by Specific
1050 Cell Types in Mouse Superficial Superior Colliculus. *J. Neurosci.* **34**, 13458–13471 (2014).

1051 43. C. Gehr, J. Sibille, J. Kremkow, Retinal input integration in excitatory and inhibitory neurons in the
1052 mouse superior colliculus in vivo. bioRxiv [Preprint] (2023).
1053 https://doi.org/10.1101/2023.04.07.536092.

1054 44. Y. K. Hong, I.-J. Kim, J. R. Sanes, Stereotyped axonal arbors of retinal ganglion cell subsets in the
1055 mouse superior colliculus. *J. Comp. Neurol.* **519**, 1691–1711 (2011).

45. C. M. Niell, M. Scanziani, How Cortical Circuits Implement Cortical Computations: Mouse Visual Cortex as a Model. *Annu. Rev. Neurosci.* **44**, 517–546 (2021).

46. H. Adesnik, W. Bruns, H. Taniguchi, Z. J. Huang, M. Scanziani, A neural circuit for spatial summation in visual cortex. *Nature* **490**, 226–231 (2012).

47. J. F. O'Rawe, Z. Zhou, A. J. Li, P. K. LaFosse, H. C. Goldbach, M. H. Histed, Excitation creates a distributed pattern of cortical suppression due to varied recurrent input. *Neuron*, doi: 10.1016/j.neuron.2023.09.010 (2023).

48. T. Baden, P. Berens, K. Franke, M. Román Rosón, M. Bethge, T. Euler, The functional diversity of retinal ganglion cells in the mouse. *Nature* **529**, 345–350 (2016).

49. M. K. Kapadia, M. Ito, C. D. Gilbert, G. Westheimer, Improvement in visual sensitivity by changes in local context: parallel studies in human observers and in V1 of alert monkeys. *Neuron* **15**, 843–856 (1995).

50. B. Krieger, M. Qiao, D. L. Rousso, J. R. Sanes, M. Meister, Four alpha ganglion cell types in mouse retina: Function, structure, and molecular signatures. *PLoS ONE* **12**, e0180091 (2017).

51. J. M. Brenner, R. Beltramo, C. R. Gerfen, S. Ruediger, M. Scanziani, A genetically defined tecto-thalamic pathway drives a system of superior-colliculus-dependent visual cortices. *Neuron* **111**, 2247-2257.e7 (2023).

52. A. Zénon, R. J. Krauzlis, Attention deficits without cortical neuronal deficits. *Nature* **489**, 434–437 (2012).

53. R. J. Douglas, C. Koch, M. Mahowald, K. A. Martin, H. H. Suarez, Recurrent excitation in neocortical circuits. *Science* **269**, 981–985 (1995).

54. K. D. Harris, T. D. Mrsic-Flogel, Cortical connectivity and sensory coding. *Nature* **503**, 51–58 (2013).

55. L. Guo, A. Kumar, Role of interneuron subtypes in controlling trial-by-trial output variability in the neocortex. *Commun. Biol.* **6**, 1–13 (2023).

56. T. Fardet, S. B. Vennemo, J. Mitchell, H. Mørk, S. Graber, J. Hahne, S. Spreizer, R. Deepu, G. Trensch, P. Weidel, J. Jordan, J. M. Eppler, D. Terhorst, A. Morrison, C. Linssen, A. Antonietti, K. Dai, A. Serenko, B. Cai, P. Kubaj, R. Gutzen, H. Jiang, I. Kitayama, B. Jürgens, H. E. Plesser, NEST 2.20.0, Zenodo (2020); https://doi.org/10.5281/zenodo.3605514.

57. D. Fürth, T. Vaissière, O. Tzortzi, Y. Xuan, A. Märtin, I. Lazaridis, G. Spigolon, G. Fisone, R. Tomer, K. Deisseroth, M. Carlén, C. A. Miller, G. Rumbaugh, K. Meletis, An interactive framework for whole-brain maps at cellular resolution. *Nat. Neurosci.* **21**, 139–149 (2018).